Evanescent absorption based fluoride fiber sensing enhancement led by doped graphene's thermo-optic dispersion in NIR

Anuj K. Sharma[1] · Ishika Sharma[1]

Abstract

Evanescent wave absorption based fiber optic sensor with fluoride core, doped silica clad, amorphous silicon layer, and graphene monolayer is studied in near infrared for highly sensitive and precise recognition of melanoma in liver tissues. The findings reveal that by carefully tuning the graphene's dispersive behavior through doping and operating at slightly increased temperature (above room temperature) can lead to significantly high sensitivity and fine resolution. An optimum combination '1550 nm wavelength, 0.6 eV chemical potential (of graphene), and 311.1 K temperature' leads to 112.211 mW/RIU sensitivity and 8.91×10^{-10} RIU resolution. An ultrathin silicon layer leads to better performance along with improved stability against possible oxidation and thermal issues. A detailed survey finds that the above performance (resolution, in particular) is largely superior than the fiber sensors based on different techniques. The proposed sensor can be amended accordingly for biomedical applications needing high precision of tissue/process monitoring.

Keywords Fluoride fiber · Sensor · Evanescent · Graphene · Thermo-optic effect · Infrared

1 Introduction

Fiber optic sensors have become integral part of a huge cluster of industrial, research, and routine applications (Hossain et al. 2016; Hu et al. 2016; Nedoma et al. 2017). Several techniques such as surface plasmon resonance (SPR) (Sharma et al. 2018), lossy mode resonance (LMR) (Paliwal and John 2015), and fluorescence spectroscopy (FS) (Benito-Peña et al. 2016) etc. have been applied to design fiber optic sensors with high sensitivity and precision of detection. The success of any fiber optic sensor lies in its sensing performance as well as the ease of design and fabrication for mass applications (e.g., remote sensing) under different (or even precarious) conditions. The above-mentioned techniques can have their certain limitations/disadvantages like complexity in depositing: uniform/corrugated metallic layers (for SPR), conducting semiconductor layers (for LMR), and

✉ Anuj K. Sharma
anujsharma@nitdelhi.ac.in

[1] Physics Division, Department of Applied Sciences, National Institute of Technology Delhi, Narela, Delhi 110040, India

florescent layers (for FS). Even if the deposition is performed conveniently, the physical/chemical stability of those layers under variable environmental conditions (e.g., temperature, humidity etc.) can be another critical issue, which brings a detrimental influence on sensor's performance.

With this background, it is worthwhile to mention that evanescent wave-absorption based fiber optic sensors (EWFOS) have also been very useful in various sensing and measurement applications (Ghahrizjani et al. 2016; Apriyanto et al. 2018). These sensors are based on the absorption of evanescent wave, which is an exponentially decaying wave generated at an interface where attenuated total reflection (ATR) occurs (Hecht 2017), by the surrounding medium (i.e., analyte). EWFOS possesses relatively easier design in which a bare fiber or the one with an absorbing clad (such as dyes that can be easily coated on the fiber core) can be used to sense an analyte, which can absorb light and will lead to change in output power emanating from the fiber end (Renganathan et al. 2011). Furthermore, EWFOS possesses advantages like independent measurements from bulk solution as penetration depth of evanescent wave is generally ten to several hundred nanometres (Vollmer and Arnold 2008; Zhong et al. 2014, 2016). Further, multiple reflections occurring in short sensing region makes it more sensitive than single point attenuated total reflection (ATR) sensors (Amezcua-Correa et al. 2007; Wang and Wolfbeis 2015; Xin et al. 2017). Furthermore, the measurement system of EWFOS is economical, portable, smart structured, and possesses good compatibility (Singh et al. 2013; Zhong et al. 2018).

The performance and stability of EWFOS can further be enhanced by using specific 2D materials (e.g., graphene), and additional absorbing layers (e.g., silicon). Importantly, monolayers of 2D materials possess high surface to volume ratio leading to greater adsorption of sensing media at their surface, which results in increased surface interaction (Varghese et al. 2015). Graphene, in particular, owns very high level of mechanical strength even at higher temperatures (Aliofkhazraei et al. 2016). Moreover, the presence of C–C bonds makes it a suitable choice in sensors aimed at the detection of biological specimens (such as tissues, DNA etc.) (Qiu et al. 2016). Silicon not only shows encouraging absorption properties in near infrared (NIR) but also has very good stability even in aqueous solutions (Singh et al. 2016).

Having discussed above possibilities, it is equally important to point out that graphene has an enormously crucial feature of tunable optical properties in terms of temperature (T), chemical potential (μ), and NIR wavelength (λ) (Aliofkhazraei et al. 2016). Silicon also shows more absorption in NIR spectral region (Singh et al. 2016). Moreover, NIR wavelengths cause much smaller photodamage to biological samples than visible light (Bixler et al. 2014). All these arguments lead us to consider NIR wavelength to avail above benefits. So, in order to design an EWFOS with graphene and silicon layers aimed at enhanced sensing performance and stability, one must select the fiber core material complying with these requirements. In this regard, fluoride glasses can be preferred because of their suitable optical properties in NIR such as small mean dispersion, negligibly smaller birefringence, lesser thermal effect, low optical non-linearity, and broad transmission window (Tao et al. 2015; Tran et al. 1984).

In the present work, we have simulated and analyzed the performance of EWFOS with fluoride glass core, silica-based clad, amorphous silicon (α-Si) layer, and graphene monolayer in NIR for detection of malignancies in liver tissues (Fig. 1). The performance of EWFOS is tuned while simultaneously tuning the temperature (T) and graphene's chemical potential (μ) at 3 different NIR wavelengths (1100 nm, 1300 nm, and 1550 nm). The prime objective of this exercise is to find out the set of parameters (i.e., T, μ, and λ) leading to as much enhanced sensing performance (in terms of sensitivity and resolution) as possible in
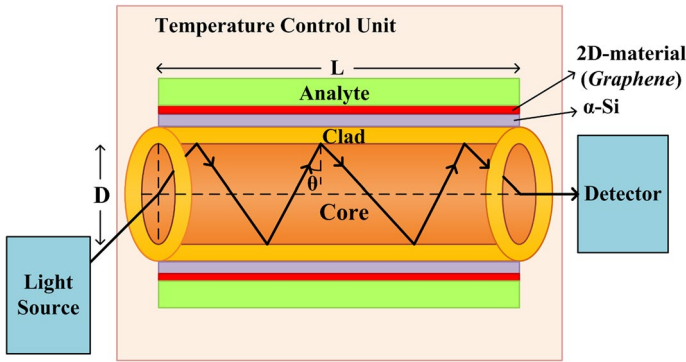
Fig. 1 Schematic representation of EW absorption based fiber optic sensor for detection of RI of healthy and cancerous liver tissues. Light is launched inside the fiber core and the variation in its intensity (after getting modulated by the sensor probe) is measured by detector at the output end. Fiber probe is placed in a unit with controlled temperature

NIR. Another objective is to test the sensor's performance under increased temperature, which provides a glimpse of sensor's thermal stability also in one way or another. The results are explained in terms of suitable physical concepts.

2 EWFOS design considerations

A schematic of the proposed EWFOS is shown in Fig. 1. We have considered the fiber core diameter (D) to be 450 μm, which is significantly greater than λ (1100–1550 nm), therefore, ray analysis is chosen for power calculations. In ray analysis, each propagating mode can be thought as a ray propagating through the fiber. The angular (or modal) power distribution for a collimated launching (i.e., light is assumed to be exactly focused on fiber axis) can be expressed as (Gupta and Singh 1994):

$$p(\theta) \propto \frac{n_{co}^2 sin\theta cos\theta}{(1 - n_{co}^2 cos^2\theta)^2} \tag{1}$$

here, θ is the angle with which light ray propagates through the fiber core (as shown in Fig. 1) and n_{co} is the fiber core refractive index (RI). Each ray suffers number of reflections ($N_{ref} = LCot\theta/D$) at the interface during its propagation within the fiber of length L (7.5 cm in the proposed work). So, the normalized output power (P) is given by (Ruddy 1990):

$$P_{out} = \frac{\int_{\theta_{cr}}^{\pi/2} R(\theta)^{N_{ref}(\theta)} p(\theta) d\theta}{\int_{\theta_{cr}}^{\pi/2} p(\theta) d\theta} \tag{2}$$

here, θ_{cr} is the critical angle ($sin^{-1}\{n_{cl}/n_{co}\}$) and n_{cl} is the RI of clad material. Further, the reflection coefficient, i.e., $R(\theta)$ is calculated by using transfer matrix method (TMM) for multilayer system (Hecht 2017). We now discuss the sensor components.

By keeping in mind the requirement of total internal reflection (TIR) {i.e., $n_{co} > n_{cl}$} at core–clad interface and greater numerical aperture (NA) to accommodate large number of

modes (angles), different core (fluoride glasses) and clad (fluoride and silica-based glasses) materials along with their λ-dependent RI values are considered (Ghatak and Thyagrajan 1998). The preliminary analysis established that ZBLA ($ZrF4_{57}BaF2_{34}LaF3_5AlF3_4$) fluoride glass core and GeO_2 (19.3%) doped silica clad (50 nm thick clad is taken in the proposed work) is the most preferred combination.

Third layer in the sensor design is an α-Si ultrathin film whose RI ($n_{\alpha\text{-Si}}$) values are adapted from Pierce and Spicer (1972). The fourth one is the graphene monolayer whose complex RI (n_{gr}) is a function of λ, μ, and T as per Kubo formulation (Aliofkhazraei et al. 2016). For experimental realization, α-Si thin layer and graphene monolayer can be deposited using chemical vapor deposition (CVD) technique (Qiu et al. 2016; Baranov et al. 2014).

As final layer, two liver tissues i.e., normal ('N') and cancerous ('HCC') are taken as analytes. Due to their dissimilar absorption and scattering characteristics, HCC and N tissues can be discriminated in terms of their complex RI (n_H and n_N, respectively), which are adapted from an earlier experimental data for λ-range of 450–1550 nm (Giannios et al. 2016). It is crucial to mention here that the data reported in the above work (Giannios et al. 2016) is not specific to bacterial phases (e.g., lag, exponential, stationary, and death phases). However, the above work reported that the cell morphology of the tissues utilized in their measurements did not change with time. It indicates that the phase of the tissue samples did not change during their measurements. Any heterogeneity due to possible influence of temperature (which is an important parameter in our study) on bacterial growth phase is not considered due to intact cell morphology of the tissue samples. Therefore, it may be assumed that the effect of temperature on the tissue samples is homogeneous and the same may be conveniently represented by the corresponding thermo-optic coefficient considered for the tissue samples (Yanina et al. 2018).

For a numerical appreciation of the RI of above-mentioned constituents of the proposed sensor, the Table 1 presents the RI values of different layers considered in the proposed work at different wavelengths (1100 nm, 1300 nm, and 1550 nm) in the temperature range 296–333 K.

The sensing method here is to correlate the variation in RI of HCC (with 'N' as reference) with the malignancy level therein. For simulation of results, MATLAB® programming tool is utilized. Sensitivity and resolution are designated to evaluate the sensor's performance. Sensitivity (S_n) is defined as the change in output power ($\delta P = P_H - P_N$) with respect to change (δn_r) in HCC tissue RI (n_r as real RI) (Ruddy 1990):

$$S_n = \left| \frac{\delta P}{\delta n_r} \right| \tag{3}$$

Resolution is defined as the smallest change in analyte RI detectable by the sensor. Mathematically, resolution (R_n) corresponding to RI of HCC tissue can be expressed as:

$$R_n = \Delta P_R \times \left| \frac{\delta n_r}{\delta P} \right| = \frac{\Delta P_R}{S_n} \tag{4}$$

Here, ΔP_R is the resolution of the photodiode used as power meter. Standard detectors have ΔP_R of the order 0.1 nW (Optical power meter kits 2019). It is worthwhile to mention that in order to achieve finer resolution of the sensor measurement, one needs to opt for correspondingly finer resolution of the photodiode, which may lead to increase in the overall cost of the sensor probe. The above cost factor may be kept in consideration during the possible practical realization of the sensor probe.

Table 1 RI values of different layers at three wavelength values (1100 nm, 1300 nm, and 1550 nm) and four temperature values (296 K, 308 K, 320 K, and 333 K). The value of µ for graphene is taken as 0.6 eV

| T (K)	$\lambda = 1100$ nm	$\lambda = 1300$ nm	$\lambda = 1550$ nm
296	$n_{co} = 1.5144$	$n_{co} = 1.5129$	$n_{co} = 1.5114$
	$n_{cl} = 1.4765$	$n_{cl} = 1.4742$	$n_{cl} = 1.4715$
	$n_{\alpha\text{-Si}} = 3.5817$	$n_{\alpha\text{-Si}} = 3.5228$	$n_{\alpha\text{-Si}} = 3.4802$
	$n_{gr} = 2.3308 + 0.2890i$	$n_{gr} = 0.3264 + 0.8236i$	$n_{gr} = 0.0929 + 2.5166i$
	$n_N = 1.3655 + 0.0030i$	$n_N = 1.3638 + 0.0028i$	$n_N = 1.3624 + 0.0027i$
	$n_H = 1.3512 + 0.0054i$	$n_H = 1.3491 + 0.0053i$	$n_H = 1.3475 + 0.0052i$
308	$n_{co} = 1.5142$	$n_{co} = 1.5127$	$n_{co} = 1.5112$
	$n_{cl} = 1.4766$	$n_{cl} = 1.4743$	$n_{cl} = 1.4716$
	$n_{\alpha\text{-Si}} = 3.5817$	$n_{\alpha\text{-Si}} = 3.5228$	$n_{\alpha\text{-Si}} = 3.4802$
	$n_{gr} = 2.3210 + 0.3006i$	$n_{gr} = 0.3345 + 0.8315i$	$n_{gr} = 0.0956 + 2.5174i$
	$n_N = 1.3613 + 0.0030i$	$n_N = 1.3595 + 0.0028i$	$n_N = 1.3582 + 0.0027i$
	$n_H = 1.3469 + 0.0054i$	$n_H = 1.3449 + 0.0053i$	$n_H = 1.3432 + 0.0052i$
320	$n_{co} = 1.5140$	$n_{co} = 1.5126$	$n_{co} = 1.5110$
	$n_{cl} = 1.4768$	$n_{cl} = 1.4745$	$n_{cl} = 1.4717$
	$n_{\alpha\text{-Si}} = 3.5817$	$n_{\alpha\text{-Si}} = 3.5228$	$n_{\alpha\text{-Si}} = 3.4802$
	$n_{gr} = 2.3111 + 0.3123i$	$n_{gr} = 0.3423 + 0.8394i$	$n_{gr} = 0.0983 + 2.5182i$
	$n_N = 1.3570 + 0.0030i$	$n_N = 1.3553 + 0.0028i$	$n_N = 1.3539 + 0.0027i$
	$n_H = 1.3427 + 0.0054i$	$n_H = 1.3406 + 0.0053i$	$n_H = 1.3390 + 0.0052i$
333	$n_{co} = 1.5138$	$n_{co} = 1.5124$	$n_{co} = 1.5108$
	$n_{cl} = 1.4769$	$n_{cl} = 1.4746$	$n_{cl} = 1.4719$
	$n_{\alpha\text{-Si}} = 3.5817$	$n_{\alpha\text{-Si}} = 3.5229$	$n_{\alpha\text{-Si}} = 3.4802$
	$n_{gr} = 2.3002 + 0.3249i$	$n_{gr} = 0.3506 + 0.8481i$	$n_{gr} = 0.1012 + 2.5192i$
	$n_N = 1.3524 + 0.0030i$	$n_N = 1.3507 + 0.0028i$	$n_N = 1.3493 + 0.0027i$
	$n_H = 1.3381 + 0.0054i$	$n_H = 1.3360 + 0.0053i$	$n_H = 1.3344 + 0.0052i$

3 Results, discussion, and interpretation

3.1 General analysis of 5-layer EWOFS for further direction

Figure 2 shows the thermal variation of S_n for four values of µ at $\lambda = 1550$ nm with (a) 10 nm, and (b) 60 nm α-Si layer. Two observations are clearly visible. First, the sensor's performance improves (i.e., greater sensitivity and finer resolution) with an increase in both T as well as µ. Noteworthy is that the S_n variation with T follows a steady pattern but the same is not the case for S_n variation with µ as there is a vast deviation among the S_n magnitudes corresponding to 0.5 eV and relatively greater µ-values. Second, the decrease in α-Si layer thickness leads to reasonably enhanced sensing performance.

Numerically, a transition of α-Si thickness from 60 to 10 nm causes a variation in maximum value of S_n from 101.512 to 113.152 mW/RIU (i.e., 11.5% enhancement). This is a good result in practical terms as an ultrathin silicon layer will also help in improving sensor's stability against possible oxidation and thermal variation. At this point, it is important to critically analyse the findings for further directives. First, the analysis needs to be carried out at more wavelengths other than 1550 nm in order to reach a broader understanding. Second, it is not always recommended to operate at higher temperatures such as 333 K,

Fig. 2 Simulated thermal variation of sensitivity (S_n) of 5-layer EWFOS for four different μ-values at λ = 1550 nm with **a** 10 nm, and **b** 60 nm thick α-Si layer. The inset shows the corresponding thermal variations of R_n
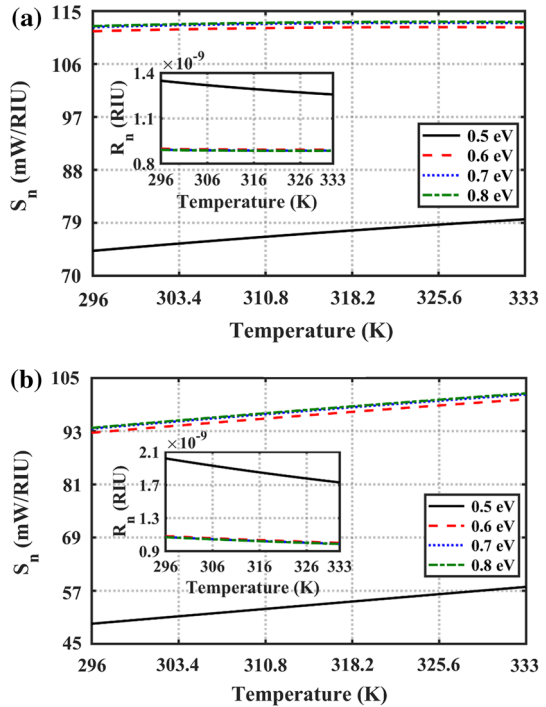

therefore, an attempt should be made to seek lower temperature values at which equally (or nearly identical) high sensing performance can be attained. Third, better performance with a decrease in α-Si layer thickness necessitates that the sensor design analysis should be carried out without α-Si layer for more clarity. The next sections cover these points in detail.

3.2 Coupled role of temperature and graphene's chemical potential at different NIR wavelengths

Figure 3 presents the simulated 2D (i.e., T–μ) variation of S_n at (a) λ = 1100 nm, (b) λ = 1300 nm, and (c) λ = 1550 nm. It can be observed from above plots that the 2D patterns of variation of S_n are significantly affected by the variation in λ, T, and μ. For detailed understanding, the Table 2 summarizes the main findings of Fig. 3.

Clearly, the maximum S_n (and hence, the finest R_n) is observed at λ = 1550 nm. However, it is interesting to note that at any λ, the effect of T and μ cannot be seen in isolation. Rather, the best values of S_n and R_n belong to three different T values with a clear indication that μ = 0.8 eV is common to all three of them. Apparently, the dispersion and thermo-optic effects in all the concerned media tune themselves in such a way that a combination of λ = 1550 nm, T = 311.6 K, and μ = 0.8 eV leads to best values of S_n and R_n. However, there is another very important point here that in all three plots, there is a discrete μ-region (over the whole T-range) where S_n hits the lowest value. More interestingly, the above region shifts to smaller μ-value for longer wavelength. Numerically, these μ-values (i.e., corresponding to minimum S_n) are 0.7 eV at λ = 1100 nm, 0.59 eV at λ = 1300 nm, and 0.49 eV at λ = 1550 nm, respectively. It suggests that while designing the EWFOS aiming at high

Fig. 3 Simulated 2D (T-μ) variation of sensitivity (S_n) of 4-layer (i.e., without α-Si layer) EWFOS at **a** λ = 1100 nm, **b** λ = 1300 nm, and **c** λ = 1550 nm
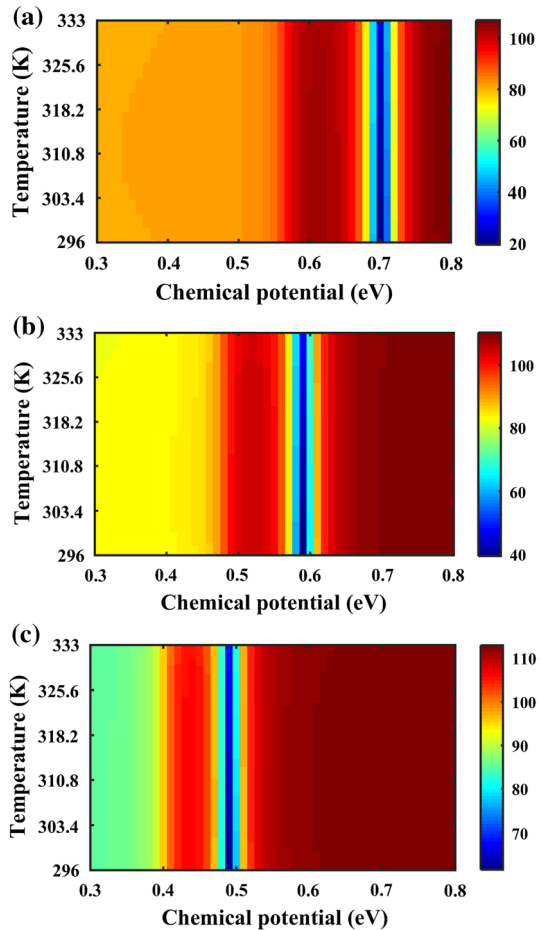
performance, one has to carefully balance the chemical potential (and, hence, graphene's doping) in conjunction with the light wavelength. The above result can be explained in terms of Kubo formulation.

3.3 Graphene's dynamic dispersive behaviour: role of doping (μ) and temperature (T) in terms of light absorption

Figure 4 shows the variation of graphene's extinction coefficient ($\kappa_{Graphene}$) with μ for 4 different temperatures at λ = 1550 nm. These plots clearly show that $\kappa_{Graphene}$ observes a dip, which has a significant dependence on λ (inset of Fig. 4). Figure 4 also shows that the μ value corresponding to this dip in $\kappa_{Graphene}$ is not affected by the variation in T. Conceptually, this dip in $\kappa_{Graphene}$ corresponds to minimum absorption by graphene monolayer, which leads to minimum variation in P_{out} eventually bringing a decrease in S_n as evident in Fig. 3. In view of longer λ to be preferred, it is also required to take greater values of μ (as is clear from Fig. 3 and Table 2). However, in practical terms, it is not easy to achieve μ of the order of 0.8 eV as it will require very high levels of doping or dynamic electrical gating

Fig. 4 Simulated variation of extinction coefficient ($\kappa_{Graphene}$) of graphene monolayer with μ for different temperatures at $\lambda = 1550$ nm. The inset shows the corresponding $\kappa_{Graphene}$ vs. μ variations for different wavelengths at T = 296 K
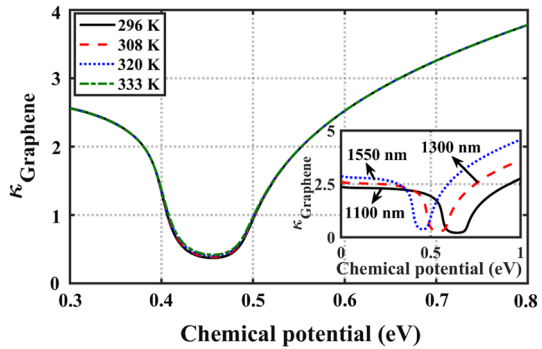

Table 2 Maximum S_n and minimum R_n with their corresponding tunable parameters (μ, T) at 3 NIR wavelengths

λ (nm)	Performance parameters		Corresponding tunables	
	Max. S_n (mW/RIU)	Min. R_n (RIU)	μ (eV)	T (K)
1100	106.933	9.35×10^{-10}	0.8	312.2
1300	110.373	9.06×10^{-10}	0.8	309.8
1550	113.036	8.85×10^{-10}	0.8	311.6
1550	112.211	8.91×10^{-10}	0.6	311.1

etc. Notably, chemical doping can perpetually adjust graphene layers for durable device applications if the value of μ is set at 0.6 eV for which the graphene layer can be considered isolated from the environment (Aliofkhazraei et al. 2016).

Hence, from practical viewpoint, the value of μ should not exceed 0.6 eV (let alone 0.8 eV), which is also favourable from the viewpoint that there is no dip in S_n at $\lambda = 1550$ nm and $\mu = 0.6$ eV. With this modified approach, if we revisit Fig. 3c, it is found that the best value of (S_n, R_n) at $\mu = 0.6$ eV and $\lambda = 1550$ nm is (112.211 mW/RIU, 8.91×10^{-10} RIU) for T = 311.1 K (shown as the shaded row in Table 2). Notably, the optimized temperature value (311.1 K) is very close to the human body temperature (310 K) (Baumann et al. 1997) which makes the proposed sensor probe an ideal candidate for malignancy detection at body temperature only. The above (S_n, R_n) is almost identical to what we achieved at $\mu = 0.8$ eV, $\lambda = 1550$ nm, and T = 311.6 K, i.e., (113.036 mW/RIU, 8.85×10^{-10} RIU).

3.4 Sensing performance comparison

A common criterion among different fiber sensor techniques (e.g., SPR, LMR etc. as discussed in Sect. 1) should be selected as resolution (in RIU) as it can be an indicator of tissue malignancy at an early stage. An extensive literature survey reveals that SPR based fiber sensors provide resolution in the range of 10^{-6}–10^{-7} RIU (Sharma et al. 2018). Further, LMR-based fiber sensors can provide resolution up to 10^{-9} RIU (Paliwal and John 2015; Arregui et al. 2016). In that sense, the proposed EWOFS is capable of providing ultrafine resolution in the range 10^{-10} RIU. Also, compared with our previous work (EW based chalcogenide fiber sensor with MoS_2 monolayer at $\lambda = 1200$ nm and room

temperature) (Sharma and Gupta 2018), the proposed EW based fluoride fiber sensor working at $\mu = 0.6$ eV, $\lambda = 1550$ nm, and $T = 311.1$ K not only betters the resolution by an order but also provides nearly 20% greater sensitivity [i.e., 112.211 mW/RIU vs. 93.7 mW/RIU (Sharma and Gupta 2018)].

4 Conclusion

EWFOS sensor with ZBLA core, doped silica clad, graphene monolayer, and amorphous silicon layer is simulated at three NIR wavelengths to resolve the malignant liver tissue. The analysis suggests that working at increased temperature, longer wavelength, and greater doping of graphene leads to sensing performance enhancement. However, from practical viewpoint, $\mu = 0.6$ eV, $\lambda = 1550$ nm, and $T = 311.1$ K can be chosen as a pragmatic combination to attain high sensitivity (112.211 mW/RIU) and fine resolution (8.91×10^{-10} RIU). An ultrathin α-Si layer is helpful in providing slightly better sensing performance plus a crucial assistance to sensor's stability. The sensor can be very useful in biomedical applications requiring high sensitivity and ultrafine precision.

References

Aliofkhazraei, M., et al.: Graphene Science Handbook: Electrical and Optical Properties. CRC Press, Boca Raton (2016)

Amezcua-Correa, A., Yang, J., Finlayson, C.E., Peacock, A.C., Hayes, J.R., Sazio, P.J.A., Baumberg, J.J., Howdle, S.M.: Surface enhanced Raman scattering using microstructured optical fibre substrates. Adv. Funct. Mater. **17**, 2024–2030 (2007)

Apriyanto, H., et al.: Comprehensive modeling of multimode fiber sensors for refractive index measurement and experimental validation. Sci. Rep. **8**(1), 1–13 (2018)

Arregui, F.J., et al.: Giant sensitivity of optical fiber sensors by means of lossy mode resonance. Sens. Actuators B Chem. **232**, 660–665 (2016)

Baranov, E.A., Khmel, S.Y., Zamchiy, A.O.: Synthesis of amorphous silicon films with high growth rate by gas-jet electron beam plasma chemical vapor deposition method. IEEE Trans. Plasma Sci. **42**(10), 2794–2795 (2014)

Baumann, S., et al.: The electrical conductivity of human cerebrospinal fluid at body temperature. IEEE Trans. Biomed. Eng. **44**(3), 220–223 (1997)

Benito-Peña, E., et al.: Fluorescence based fiber optic and planar waveguide biosensors. A review. Anal. Chim. Acta **943**, 17–40 (2016)

Bixler, J.N., et al.: Assessment of tissue heating under tunable near-infrared radiation. J. Biomed. Opt. Lett. **19**(7), 070501 (2014)

Ghahrizjani, R., et al.: A novel method for on line monitoring engine oil quality based on tapered optical fiber sensor (TOFS). IEEE Sens. J. **16**(10), 3551–3555 (2016)

Ghatak, A., Thyagrajan, K.: Introduction to Fiber Optics. Cambridge University Press, Cambridge (1998)

Giannios, P., et al.: Visible to near-infrared refractive properties of freshly-excised human-liver tissues: marking hepatic malignancies. Sci. Rep. **6**, 27910 (2016)

Gupta, B.D., Singh, C.D.: Fiber-optic evanescent field absorption sensor: a theoretical evaluation. Fiber Integr. Opt. **13**(4), 433–443 (1994)

Hecht, E.: Fifth Edition Optics. Pearson, London (2017)

Hossain, M.A., et al.: Optical fiber smartphone spectrometer. Opt. Lett. **41**(10), 2237–2240 (2016)

Hu, T., et al.: Fiber optic SPR sensor for refractive index and temperature measurement based on MMF-FBG-MMF structure. Sens. Actuators B Chem. **237**, 521–525 (2016)

Nedoma, J., et al.: Non-invasive fiber optic probe encapsulated into PolyDiMethylSiloxane for measuring respiratory and heart rate of the human body. Adv. Electr. Electron. Eng. **15**(1), 93–100 (2017)

Optical power meter kits, https://www.thorlabs.com/newgrouppage9.cfm?objectgroup_id=4216. Last accessed on 11 Jan 2019

Paliwal, N., John, J.: Lossy mode resonance (LMR) based fiber optic sensors: a review. IEEE Sens. J. **15**(10), 5361–5371 (2015)

Pierce, D.T., Spicer, W.E.: Electronic structure of amorphous Si from photoemission and optical studies. Phys. Rev. B **5**(8), 3017–3029 (1972)

Qiu, H., et al.: Evanescent wave absorption sensor based on tapered multimode fiber coated with monolayer graphene film. Opt. Commun. **366**, 275–281 (2016)

Renganathan, B., et al.: Gas sensing properties of a clad modified fiber optic sensor with Ce, Li and Al doped nanocrystalline zinc oxides. Sens. Actuators B Chem. **156**(1), 263–270 (2011)

Ruddy, V.: An effective attenuation coefficient for evanescent wave spectroscopy using multimode fiber. Fiber Integr. Opt. **9**(2), 143–151 (1990)

Sharma, A.K., Gupta, J.: Fiber optic sensor' s performance enhancement by tuning NIR wavelength, polarization, and 2D material. IEEE Photonics Technol. Lett. **30**(12), 1087–1090 (2018)

Sharma, A.K., et al.: A review of advancements (2007–2017) in plasmonics-based optical fiber sensors. Opt. Fiber Technol. **43**, 20–34 (2018)

Singh, S., Mishra, S.K., Gupta, B.D.: SPR based fibre optic biosensor for phenolic compounds using immobilization of tyrosinase in polyacrylamide gel. Sens. Actuators B **186**, 388–395 (2013)

Singh, N., et al.: Mid-IR absorption sensing of heavy water using a silicon-on-sapphire waveguide. Opt. Lett. **41**(24), 5776–5779 (2016)

Tao, G., et al.: Infrared fibers. Adv. Opt. Photonics **7**, 379–458 (2015)

Tran, D.C., et al.: Heavy metal fluoride glasses and fibers: a review. J. Light. Technol. **2**(5), 566–586 (1984)

Varghese, S., Swaminathan, S., Singh, K., Mittal, V.: Two-dimensional materials for sensing: graphene and beyond. Electronics **4**(3), 651–687 (2015)

Vollmer, F., Arnold, S.: Whispering-gallery-mode biosensing: label-free detection down to single molecules. Nat. Methods **5**(7), 591–596 (2008)

Wang, X.D., Wolfbeis, O.S.: Fiber-optic chemical sensors and biosensors (2013–2015). Anal. Chem. **88**(1), 203–227 (2015)

Xin, X., et al.: High-sensitivity four-layer polymer fiber-optic evanescent wave sensor. Biosens. Bioelectron. **91**, 623–628 (2017)

Yanina, I.Y., Lazareva, E.N., Tuchin, V.V.: Refractive index of adipose tissue and lipid droplet measured in wide spectral and temperature ranges. Appl. Opt. **57**(17), 4839–4848 (2018)

Zhong, N., et al.: A fiber-optic sensor for accurately monitoring biofilm growth in a hydrogen production photobioreactor. Anal. Chem. **86**(8), 3994–4001 (2014)

Zhong, N., Zhao, M., Zhong, L., Liao, Q., Zhu, X., Luo, B., Li, Y.: A high-sensitivity fiber-optic evanescent wave sensor with a three-layer structure composed of Canada balsam doped with GeO_2. Biosens. Bioelectron. **85**, 876–882 (2016)

Zhong, N., Chen, M., Chang, H., et al.: Optic fiber with Er^{3+}:$YAlO_3$/SiO_2/TiO_2 coating and polymer membrane for selective detection of phenol in water. Sens. Actuators B **273**, 1744–1753 (2018)